Hindawi
Advances in Materials Science and Engineering
Volume 2022, Article ID 8260107, 20 pages
https://doi.org/10.1155/2022/8260107

Research Article

Experimental and Numerical Investigation of Energy Evolution Characteristic of Granite considering the Loading Rate Effect

Feiyue Sun,[1] Junqi Fan ,[2] Jiaqi Guo ,[1] and Xiliang Liu[1]

[1]*School of Civil Engineering, Henan Polytechnic University, Jiaozuo 454003, Henan, China*
[2]*Research Institute for National Defense Engineering of Academy of Military Science PLA China, Luoyang 471023, Henan, China*

Correspondence should be addressed to Jiaqi Guo; gjq519@163.com

Received 21 July 2022; Accepted 18 August 2022; Published 20 September 2022

Academic Editor: Depeng Ma

In order to investigate the loading rate effect of energy evolution in granite, the indoor physical simulation test of single face fast unloading-three directions and five faces stress-vertical continuous loading under different loading rates was conducted using a new true triaxial rockbursttest system. The energy accumulation-dissipation-release characteristics in the process of rock deformation and failure were revealed. Based on the three-dimensional discrete element theory and the polycrystalline modeling technique (randomly generated Voronoi mineral grains), the entire process of rockburst inoculation-occurrence-development, as well as the energy evolution characteristics under true triaxial single face unloading conditions, were studied. The test results indicate that the energy transport and conversion of rock samples under different loading rates exhibit distinct stage characteristics. It can be divided into the initial energy accumulation stage, steady energy accumulation stage, rapid energy dissipation stage, and rapid energy release stage. With a rise in loading rate, the specimen in the process of energy accumulation is accompanied by energy dissipation, more external input energy, and elastic strain energy release amount into the kinetic energy of fragments, resulting in the rockburst phenomenon. As the loading rate increases, the elastic strain energy conversion rate (U_e/U) falls, while the dissipative energy conversion rate (U_d/U) increases. The higher the elastic strain energy conversion rate and the lower the dissipative energy conversion rate, the more serious the rockburst occurs. Numerical simulation results show that the entire process of rockburst inoculation-occurrence-development is successfully simulated using the crystal scale fine model (CSFM) considering the grain mineral composition. The ejection failure process can be divided into four stages, including grains ejection, rock spalling into plates, rock shearing into fragments, and rock fragments ejection. The relationships between the peak strength, elastic strain energy of rock samples, and loading rates are obtained, which is consistent with the laboratory test results. The high rate linear growth of kinetic energy evolution between the two inflection points can provide precursor information for rockburst prediction.

1. Introduction

With the competitive development of underground engineering construction, the excavation and boring speed of mines, large underground cavern groups, and tunnels (caves) have been accelerated, causing changes in the loading rate of surrounding rock mass in front of the working face. As a result, the mechanical properties of surrounding rock mass are changed, which in turn induces dynamic geological disasters such as rockburst, bringing high safety risks to the operators, and construction equipment in underground engineering. Rock dynamic response is essentially the outcome of energy drive exceeding the energy storage limit, based on the energy evolution mechanism that can reflect the dynamic process of rock failure [1–3]. According to studies, the loading rate is a significant factor in determining the occurrence of rockburst, and different loading rates have significant influences on the failure mode, strength characteristics, and energy evolution characteristics of the rock. Therefore, it is of theoretical importance and engineering application value to study the energy transport and conversion in the process of rock deformation and failure under different loading rates, as well as to reveal the essential characteristics of rock deformation

and failure, so as to enrich the dynamic response mechanism of rock.

Studies on the loading rate effect on the energy evolution of rockburst process features have received a great deal of interest from professionals in rock mechanics and engineering researchers around the world. In an experimental study, Chen et al. investigated the energy dissipation of fragments during rockburst [4]. Polito and Moldenhauer were involved in a novel method used to reveal the evolution and distribution law of elastic energy and dissipated energy density of rock samples [5]. Weyher et al. investigated the law of change in critical strain energy density [6]. Lu et al. investigated the effects of loading rate on rock deformation, strength, failure mode, and energy evolution [7]. Si et al. studied the influence of loading rate on the energy evolution of rockburst damage mechanism in circular tunnels [8]. The abovementioned research has significantly advanced the development of mechanical properties and energy evolution characteristics of rocks under different loading rates. However, the results achieved so far are primarily in uniaxial, biaxial, and conventional triaxial compression conditions to carry out research on energy transport and conversion in the process of rock deformation and failure, resulting in its difficulty in effectively simulating the real stress path and boundary condition transformation process of surrounding rock mass before and after excavation. Therefore, it is imperative to conduct research on the energy evolution characteristics of the loading rate effect on rockburst process under the true triaxial test conditions. In the aspect of numerical simulation, Zhang et al. studied the rock inner failure mechanisms under different loading rates based on the particle discrete element model [9]. Lee et al. developed a novel energy damage model based on continuum damage mechanics [10]. Ma et al. simulated laboratory experiments on coal-rock composite samples using the particle flow code [11]. Yu et al. studied the influence of loading rate on rock energy evolution and failure mode [12]. Most of the abovementioned results focus on the simulation of the rock static failure process, while there are few studies on the simulation of the dynamic failure process of rockburst reported in the literature, especially the numerical simulation of rock fragmentation ejection process based on polygonal crystal structure is still in a blank state, making it difficult to accurately reflect the physical reality of rock and to reasonably simulate the dynamic disaster of rockbursts at the engineering scale. Therefore, this paper adopts a computational grid based on a randomly distributed Voronoi diagram and discretizes the Voronoi polygon of rock mineral grain shape. In the entire process of simulating the ejection failure of rock fragments, the grid dependence of the model mechanical parameters on the general discrete element method is largely eliminated. It can accurately simulate the stress-strain curve and strength nonlinear characteristics of rocks, demonstrate the entire process of rockburst disaster, and reveal the inoculation mechanism of rockburst disaster.

This paper uses the new true triaxial rockburst test system, according to the new rockburst test method, new loading and unloading path to conduct physical simulation tests of single face fast unloading-three direction and five faces stress-vertical continuous loading under different loading rates. The influence of loading rate on the energy evolution characteristics during rock deformation and failure process is analyzed. Based on the energy principle, the transformation mechanism of energy storage, accumulation, dissipation, and release in each stage of rock deformation and failure under different loading rates is expounded. The study combines experimental results with the coupling of three-dimensional discrete element numerical analysis method and polycrystalline modeling theory (randomly generated Voronoi mineral grains) to construct a crystal scale fine model (CSFM) considering the composition of mineral grains. The entire process of rockburst inoculation-occurrence-development and the energy evolution characteristics under true triaxial single face unloading conditions are studied from the macro and micro levels. The study results to provide a fundamental scientific basis and significant theoretical support for the occurrence mechanism and prediction of rockbursts in underground engineering under high-stress states.

2. Test Equipment and Methods

2.1. Test Equipment. The test system mainly consists of true triaxial rockburst testing machine, loading system, control system, real-time data signal acquisition and monitoring system, high-speed camera system, and other subsystems (Figure 1). True triaxial rockburst testing machine is a new high-pressure servo rigid press, the maximum vertical loading pressure of 5000 kN, the maximum horizontal loading pressure of 3000 kN, through the full digital servo controller control can be realized in three vertical directions for independent loading and unloading. It has the special function of single face fast unloading under the three directions and six faces loading conditions. It can accurately simulate the process of rapid change of surrounding rock stress path at the moment of underground engineering excavation. With the aid of a high-speed camera, it is possible to observe the failure phenomenon of unloading faces in real-time.

2.2. Rock Samples Preparation. Grayish–white granite samples were collected in Wenshang County, Shandong Province, China (Figure 2). To ensure the comparability of tests and decrease the impact of material heterogeneity and dispersion on the test results, all specimens were extracted from the same intact rock. Before true-triaxial rockburst tests, the rectangular prismatic specimens, 100 mm (length) × 100 mm (width) × 200 mm (height), were prepared, and all sides and ends of specimens were finely ground and polished to minimize the local stress concentration and produce flat and smooth end surfaces. To ensure that rock samples are uniformly pressured in all directions, the processing accuracy is strictly in accordance with the standard of the International Society for Rock Mechanics [13], with a flatness error of ±0.05 mm for two opposite faces and a perpendicularity error of ±0.25° for two adjacent faces.

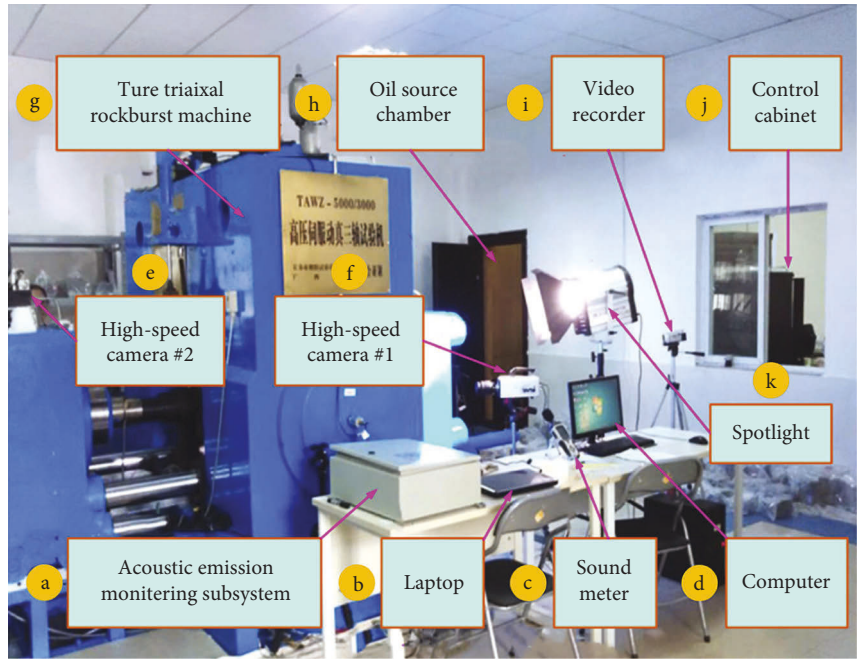

Figure 1: True triaxial rockburst testing system.

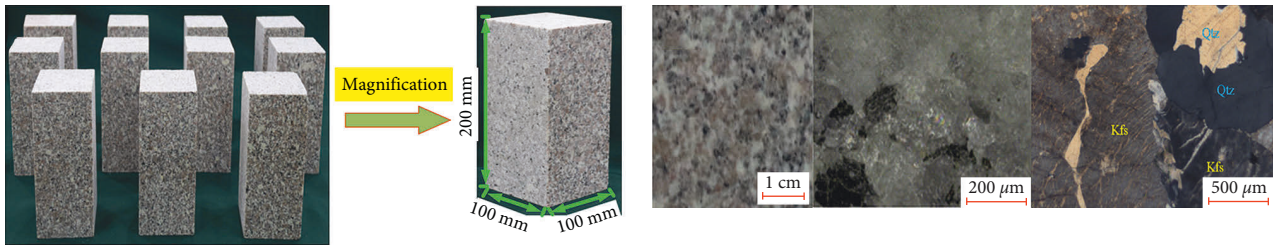

(a) (b)

Figure 2: Photo and microstructure of sample. (a) Photo of rock specimens; (b) naked-eye observations (left), 3D hyper-focal distance microscopic images (middle), and optical cross-polarized micrographs (right) of granite.

2.3. Test Methodology

2.3.1. Stress Path Design. Before excavation of the cavern, the rock mass is in a triaxial stress state. After the cavern excavation is unloaded, the unloading face of rock mass appears, and its radial stress decreases sharply (the corresponding principal stress is σ_3), the tangential stress increases gradually (the corresponding principal stress is σ_1), and the principal stress along the cavern axis remains the same as the initial stress field (the corresponding principal stress is σ_2), as depicted in Figure 3. For the rock unit in the area of concentrated compressive stress in the surrounding rock mass, the radial stress on the excavation boundary is zero, while the radial stress in the rock mass at a certain distance from the excavation surface rises sharply along the diameter direction, and the rock unit is in a special stress state of "one face zero load-three direction and five faces load."

According to the stress path and boundary condition transformation process of the surrounding rock mass after excavation of an underground cavern (Figure 3), the true triaxial rockburst test with single face fast unloading-three directions and five faces stress-vertical continuous loading can accurately reproduce the stress transformation process of radial stress plunge and tangential stress concentration after excavation and unloading of deep underground engineering. In addition, engineering practice demonstrates that rockburst typically occurs within 1~3 days after excavation [14, 15], indicating that the gradual concentration of tangential stress is one of the main factors leading to rockburst. Consequently, the process of continual concentration of tangential stress can be reproduced with vertical continuous loading. Figure 4 depicts the test method and loading-unloading path.

The specific testing procedures are described as follows: (I) The initial stress state of underground engineering rock mass before excavation is simulated according to the in-situ stress field inversion of measured geostress in a project, and the initial stress state in three directions is $\sigma_1/\sigma_2/\sigma_3 = 74.58/54.96/39.51$ MPa [17]. To achieve the loading and unloading in the tests, the values of σ_1, σ_2, and σ_3 under the initial ground stress condition in loading paths were set as 75, 55,

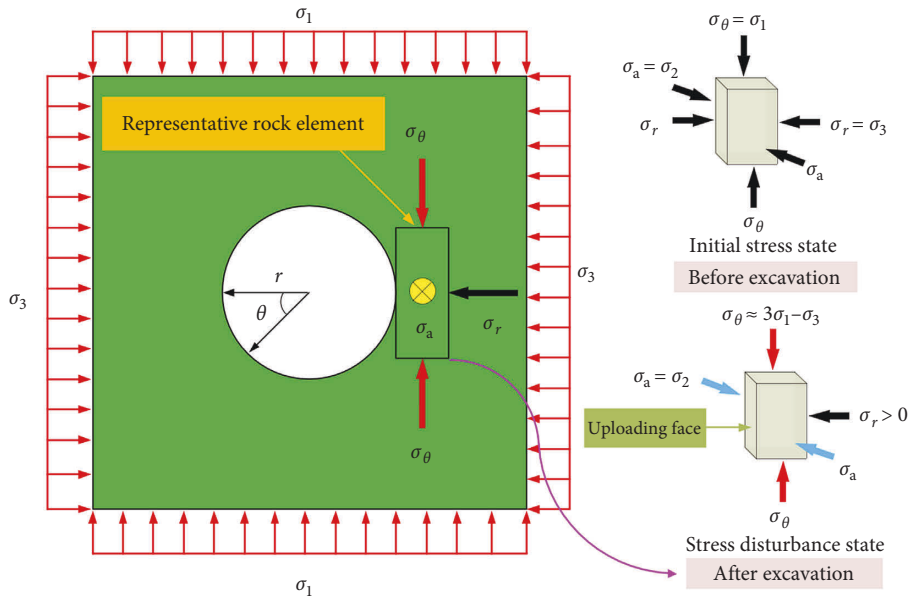

FIGURE 3: Mechanical environment of rock specimen in underground engineering before and after excavation: σ_1, σ_2, σ_3 are initial stresses, and $\sigma_1 > \sigma_2 > \sigma_3$; σ_θ, σ_a, and σ_r are stresses acting on representative rock specimen, and $\sigma_\theta > \sigma_a > \sigma_r$ (adapted from Su et al. [16]).

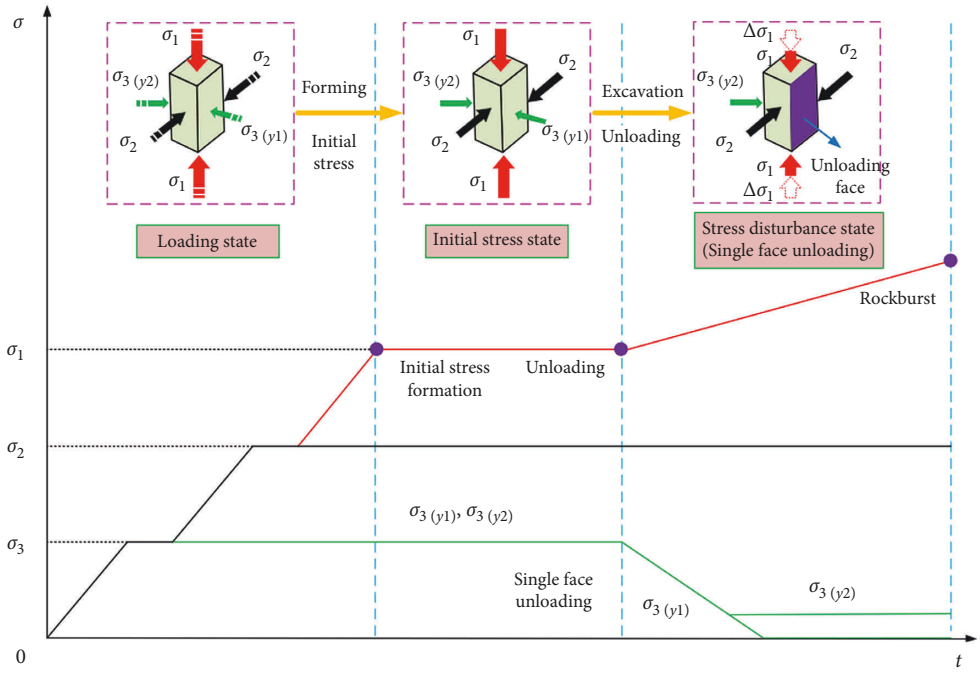

FIGURE 4: Sketch map of test method and loading-unloading path of rockburst.

and 40 MPa, respectively. Firstly, the principal stresses σ_1, σ_2, and σ_3 were loaded simultaneously to the predetermined values and then held for about 2~3 minutes. Secondly, the principal stresses σ_1 and σ_2 were loaded simultaneously to the predetermined values and then held for about 2~3 minutes. Finally, the principal stress σ_1 was loaded to the predetermined values. After the initial stress state is applied, the specimen is stabilized for approximately 6~8 minutes under the triaxial stress state of $\sigma_1 = 75$ MPa, $\sigma_2 = 55$ MPa, $\sigma_3 = 40$ MPa. (II) A single face fast unloading device (two springs) is used to unload the stress $\sigma_{3(y1)}$ to zero on one face in the Y-direction, while rapidly reducing the stress $\sigma_{3(y2)}$ to a predetermined value on the other face in the Y-direction. In order to simulate the radial stress reduction after excavation unloading in underground engineering, and to realize the conversion process the stress path and boundary conditions near the excavation boundary are under the effect of tangential stress. The stress $\sigma_{3(y2)}$ on the opposite face of the unloading face and the stress σ_2 in the X-direction are kept unchanged. Finally, the stress σ_2 in the vertical stress σ_1 is

continuously increased at different loading rates until the specimen is failure.

2.3.2. Testing Plan. In this experimental, four different loading rates of 0.05, 1.0, 3.0, and 5.0 MPa/s were designed, with strain rates of 1.7×10^{-6}, 3.4×10^{-5}, $1.0\times10^{-4,}$ and $1.7\times10^{-4}\,s^{-1}$ corresponding to the four different loading rates. The specific test procedures are detailed in Table 1. In our test, at least three specimens were prepared for each test with a given loading path to guarantee the repeatability of the experimental results. The typical failure process of each tested specimen was chosen to investigate the rockburst.

3. Stress-Strain Curve and Failure Mode of Granite Specimen

The stress-strain curves and failure modes of granite specimens with different loading rates are shown in Table 2.

Compared to the stress-strain curve of rock samples with static brittle failure rock sample no. *Z*-1, the typical stress-strain curve of rock sample with ejection failure has the following characteristics: (1) The failure process of rock samples under different loading rates roughly goes through four stages: the initial compaction stage (*OA*), the elastic deformation stage (*AB*), the prepeak unstable fracture stage (*BC*), and the postpeak failure stage (*CD*). (2) The prepeak curve has an obvious yield point, and the stress-strain curve between the yield point and the peak point changes more gently, corresponding to the splitting failure phenomena at the unloading face of rock samples and shear failure phenomena in the range of potential rockburst pits.

There is a correlation between the failure mode of granite specimens and the loading rate, and the failure mode characteristics of specimens vary depending on the different loading rates. *Z*-1 specimens display a relative rock plate splitting face on the unloading face, a large penetrating shear diagonal fracture on the inside of the rock body, and shear-tension fractures close to the unloading face, predominantly in the form of stable and slow slabbing failure. The failure modes of *Z*-2~*Z*-4 rock samples exhibit obvious multi-divisional failure characteristics, such as V-shaped or step-shaped rockburst pits, splitting cracks caused by tension appearing on the unloading face, and an uneven surface of rockburst pits.

4. Loading Rate Effect on Energy Evolution of Granite

4.1. Principle of Energy Analysis. The deformation and failure of rocks are mostly caused by energy-driven. From the viewpoint of energy, when a rock is deformed by an external force, assuming that the physical process has no heat exchange with the outside world, the total input energy generated by the external work is *U*. According to following energy conservation law [18]:

$$U = U_d + U_e, \tag{1}$$

Table 1: Testing plan.

Specimen no.	Loading rate (MPa/s)	σ_2 (MPa)	$\sigma_{3(y2)}$ (MPa)
Z-1	0.05	55	5
Z-2	1.0	55	5
Z-3	3.0	55	5
Z-4	5.0	55	5

where: U_d is the rock dissipation energy, which is used to generate internal damage and plastic deformation of rock, as depicted in the empty space encompassed by the curve in Figure 5; U_e is the rock releasable elastic strain energy, as depicted in the shaded area enclosed by the curve in Figure 5.

The total input energy *U*, elastic strain energy U_e, and dissipation energy U_d of a rock sample in the true triaxial stress state are calculated as follows [18]:

$$\begin{aligned} U &= \int_0^{\varepsilon_1} \sigma_1 d\varepsilon_1 + \int_0^{\varepsilon_2} \sigma_2 d\varepsilon_2 + \int_0^{\varepsilon_3} \sigma_3 d\varepsilon_3, \\ U_e &= \frac{\left[\sigma_1^2 + \sigma_2^2 + \sigma_3^2 - 2\nu\left(\sigma_1\sigma_2 + \sigma_2\sigma_3 + \sigma_1\sigma_3\right)\right]}{2E}, \\ U_d &= U - U_e, \end{aligned} \tag{2}$$

where: $\sigma_1, \sigma_2, \sigma_3$ is the maximum, intermediate, and minimum principal stress, respectively; $\varepsilon_1, \varepsilon_2, \varepsilon_3$ is the maximum, intermediate, and minimum principal strains, respectively; *E* is the initial elastic modulus; ν is the Poisson's ratio.

Based on the energy evolution mechanism in the process of rock deformation, the difference between dynamic and static rock failure is explained in detail [18]: due to the high-stress action of excavation unloading and disturbance load on the rock, a part of the rock is damaged intensifies in a very short time and its strength gradually decreases, while the elastic strain energy stored in the majority of rock rapidly reaches its limit value. When U_e reaches U_0 (the energy required for rock failure), i.e. $U_e = U_0$, U_e is completely released and the rock static fails. When $U_e > U_0$, the rock dynamic failure, the energy difference $\Delta U = U_e - U_0$ constitutes the kinetic energy to split the rock, inducing rockburst to occur.

4.2. Energy Evolutionary Process of Rockburst

4.2.1. Energy Evolution Characteristics of Specimens under Different Loading Rates. Using the energy calculation method in Section 4.1, the total input energy *U*, elastic strain energy U_e, dissipation energy U_d evolutionary process of granite rockburst test under different loading rates was obtained, as shown in Figure 6.

As can be seen from Figure 6, (a) The deformation and failure of rock is a dynamic imbalance process by energy-driven. The process of specimen deformation and failure under different loading rates is accompanied by energy input, accumulation, dissipation, and release. (b) Initial compression stage (stage I): The external energy input is utilized mostly for initial crack closure, frictional slip, etc. The total energy curve and the elastic strain energy curve

Table 2: Stress-strain curve and failure mode of granite specimens with different loading rates.

Loading rate (MPa/s)	Axial stress-strain curve	Peak stress (MPa)	Failure mode
0.05 (*Z*-1)	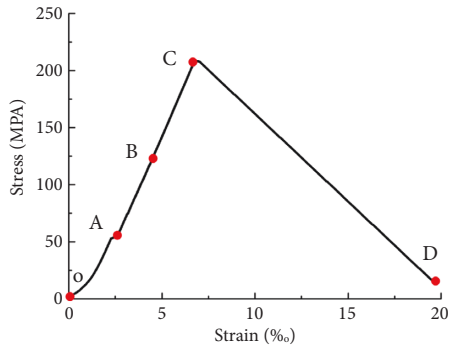	208.93	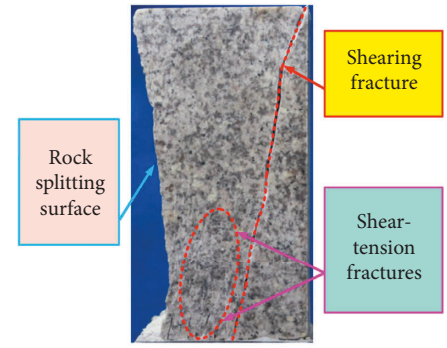
1.0 (*Z*-2)	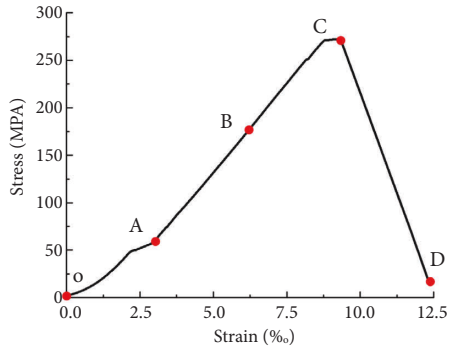	272.40	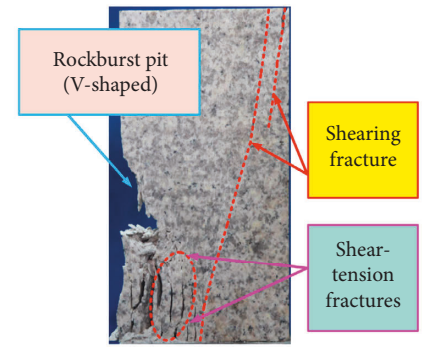
3.0 (*Z*-3)	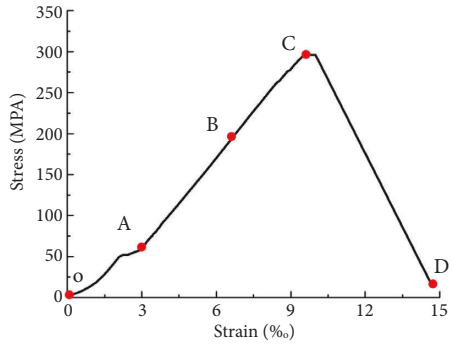	296.52	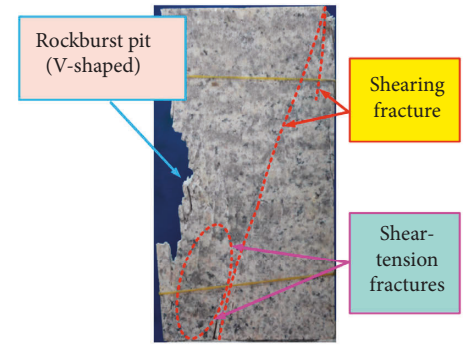
5.0 (*Z*-4)	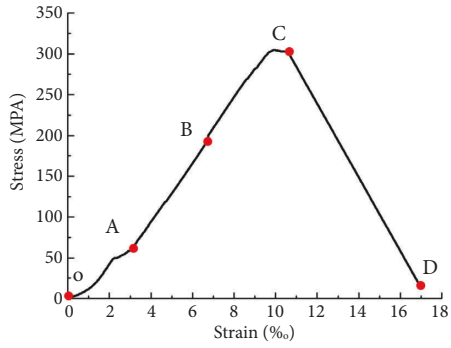	304.90	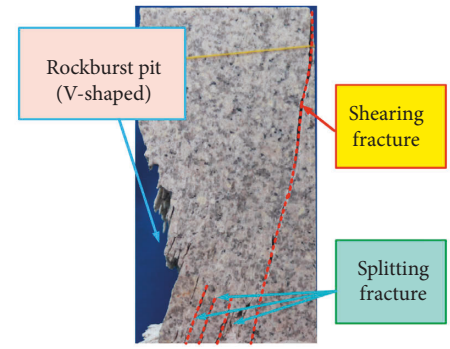

basically coincide, and the dissipation energy is close to zero, showing that the internal damage to the specimen at this stage is negligible. (c) Elastic deformation stage (stage II): With the continuous input of external energy, the microcracks inside the specimen begin to sprout, expand, and penetrate, and the dissipation energy begins to increase slowly. The total energy and elastic strain energy are positively correlated with the loading rate and are mainly stored in the specimen in the form of elastic strain energy. It indicates that the higher the loading rate is, the more obvious the brittle failure characteristics of specimen are, and the more complete the dynamic damage process is. (d) Prepeak unstable fracture stage (stage III): The accumulation capacity and rate of elastic strain energy are significantly greater than

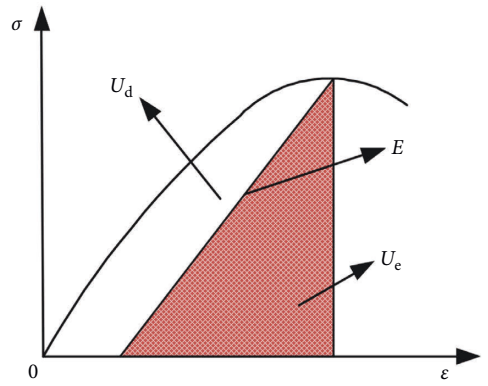

Figure 5: Stress-strain relation curve of rock [18].

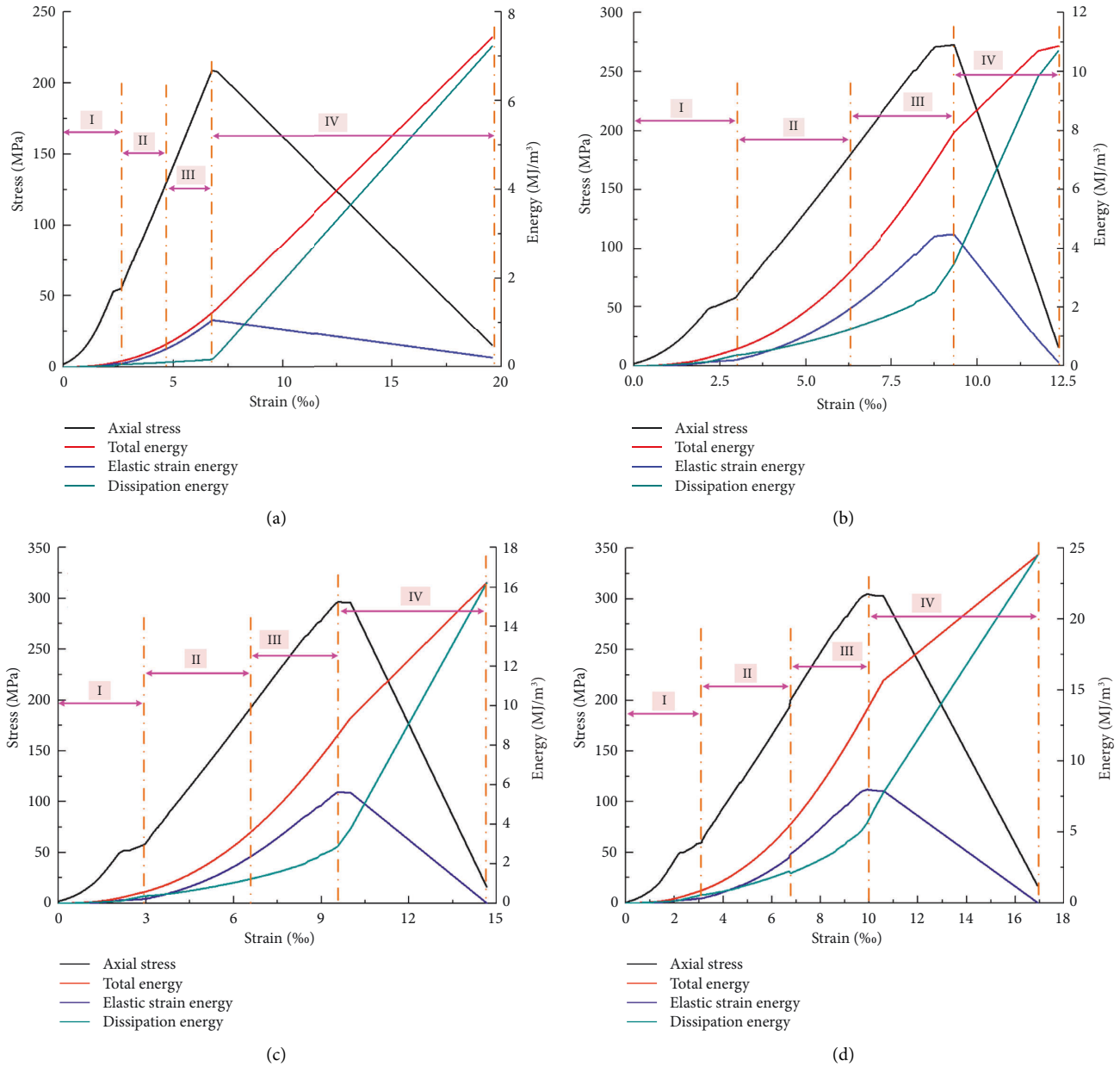

Figure 6: Energy evolution process of specimen with different loading rates during rockburst. (a) 0.05 MPa/s; (b) 1.0 MPa/s; (c) 3.0 MPa/s; and (d) 5.0 MPa/s.

the dissipation energy, and as the loading rate increases, the difference between the two values gradually increases. It indicates that the energy behavior of the specimen during prepeak stress process is primarily energy accumulation, and a part of the elastic strain energy is converted into fragment ejection kinetic energy in a small proportion, and the majority of elastic strain energy is converted into dissipation energy of rock cracking and sliding, and particle ejection begins to occur on the unloading face of specimen. (e) Postpeak failure stage (stage IV): When the peak stress is reached, the elastic strain energy curve decreases linearly while the dissipation energy curve increases linearly. This is mainly due to the instantaneous release of elastic strain energy accumulated in the specimen before the peak, and the dissipation energy increases sharply, leading to the formation of a macroscopic rupture surface through the crack and the destabilization of the specimen. It indicates that the energy behavior of specimen failure process is mainly reflected by energy release and energy dissipation. For specimen Z-1, the unloading face appears to be stable and slow slabbing failure. For other specimens, the fragments in the unloading face ejected at a relatively fast rate, and a rockburst dynamic disaster occurred. This further indicates that only a very small portion of the elastic strain energy stored before the peak of the specimen during the rockburst is converted into kinetic energy for fragment ejection, and the majority of the elastic strain energy is converted into fragment dissipation energy during the rockburst ejection failure.

From the aforementioned experimental tests, it is evident that the elastic strain energy increases gradually as the loading rate increases, the greater the accumulation of elastic strain energy, the greater the susceptibility of rockburst. It can be seen that the loading rate has a significant impact on the energy accumulation, so it is necessary to convert the loading rate under the laboratory scale to the speed of the working face under the engineering scale, take appropriate measures to reduce the elastic strain energy accumulated in the surrounding rock mass, and gradually release the energy in the surrounding rock mass to reduce the possibility of rockburst.

4.2.2. Energy Evolution Law at the Peak Stress of Specimen under Different Loading Rates. Figure 7 depicts the variation laws of total energy, elastic strain energy, and dissipation energy at the peak stress of the specimen under different loading rates. Table 3 displays the mathematical expressions of each energy characteristic value with the loading rate at the peak stress, where r denotes the loading rate.

As shown in Figure 7 and Table 3, (a) at the peak stress, the correlation coefficient values for each energy characteristic and the loading rate are all 0.999 (near to 1), showing a strong association. The change curve of elastic strain energy with an increase in loading rate exhibits a sharp increase followed by a slow rise. The overall change trend of total energy and dissipation energy curve is more similar, exhibiting a sharp increase followed by a short decline and then a sharp increase, with a cut-off value in the range of 1~3 MPa/s. (b) For the peak analysis of each energy characteristic, the elastic strain

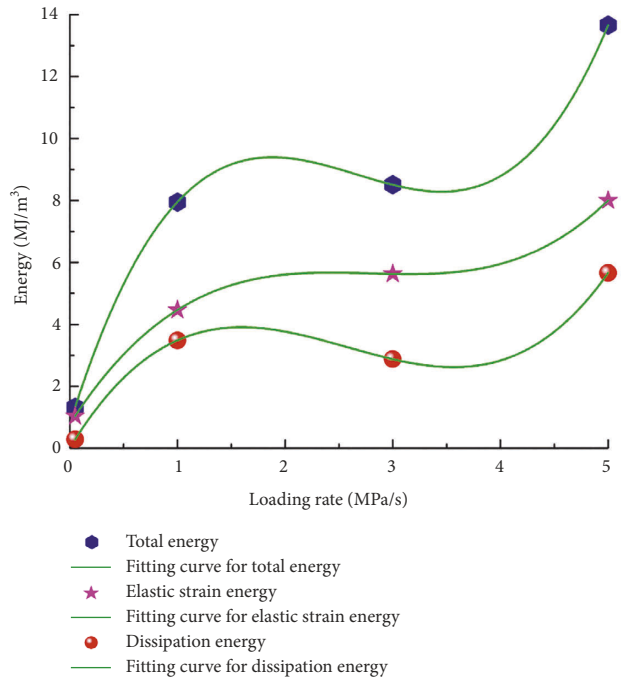

Figure 7: Energy variation characteristics at the peak value of specimen with different loading rates.

energy accumulation capacity, and the dissipation energy release capacity of the specimen are closely related to the loading rate effect. With a rise in loading rate, the specimen in the process of energy accumulation is accompanied by dissipation energy, more external input energy, and elastic strain energy released into the kinetic energy of breaking rock block, resulting in rockburst phenomenon. In addition, the greater the loading rate, the more pronounced the fracture traces remaining on the specimen failure surface, the more fully developed the through cracks, the more obvious the brittle failure characteristics, and the greater the failure strength. (c) Under different loading rates, the dissipation energy is significantly less than elastic strain energy. The lower the loading rate, the slower the expansion rate of specimen internal microfractures development. The longer the specimen damage accumulation time, resulting in the higher degree of internal deterioration of the specimen. When the loading rate progressively increases, it accelerates the expansion rate of microcracks and reduces their expansion time, so their development and expansion in a short period of time is insufficient. Therefore, raising the loading rate will minimize the degree of damage deterioration inside the rock, which is the fundamental reason for the regular variation of elastic strain energy and dissipative strain energy at the peak with the loading rate.

4.3. Energy Conversion Characteristics of Rockburst

4.3.1. Energy Conversion Characteristics of Specimens under Different Loading Rates. U_e/U is defined as the energy storage limit of rock, which is used to characterize the ability of the rock to release elastic strain energy during the

Table 3: Mathematical expression of energy eigenvalue and loading rate.

Name	Fitting curve	Correlation coefficient
Total energy	$U = 0.574r^3 - 4.594r^2 + 11.191r + 0.776$	0.999
Elastic strain energy	$U_e = 0.237r^3 - 1.986r^2 + 5.439r + 0.773$	0.999
Dissipation energy	$U_d = 0.337r^3 - 2.609r^2 + 5.752r + 0.003$	0.999

postpeak stage. The greater the rock's energy storage capacity, the less susceptible it is to energy-driven failure. U_d/U is defined to characterize the energy dissipation capability of rock. The higher the ratio, the easier the damage occurs inside the rock and the lower the energy storage capacity. Figure 8 depicts the energy conversion characteristics of the true triaxial rockburst test with different loading rates. Table 4 displays the energy values at the peak stress of specimens with different loading rates.

As shown in Figure 8 and Table 4, (a) The elastic strain energy conversion rate (U_e/U) decreases with increasing loading rate, whereas the dissipative energy conversion rate (U_d/U) increases with increasing loading rate. The average elastic strain energy conversion rate is 60.40%, whereas the average dissipative energy conversion rate is 39.60%, indicating that the elastic strain energy conversion rate is significantly greater than the dissipative energy conversion rate. Furthermore, combined with the failure mode of specimen can achieve the Z-2 specimen unloading faces V-shaped or step-shaped rockburst pits and its surface unevenness is much smaller than that of the *Z*-4 specimen. This demonstrates that in the rockburst test, the greater the elastic strain energy conversion rate and the lower the dissipation energy conversion rate, the more serious the rockburst. (b) As the loading rate increases, the development of microcrack expansion is insufficient, and the accumulation of elastic energy will be released in the form of particle ejection or fragmentation exfoliation, the greater the energy released when the rock is failure. This also demonstrates that the higher the loading rate is, the less the energy consumption of crack development and propagation of rock samples is, resulting in more elastic strain energy that can be converted into fragment ejection kinetic energy, leading to the occurrence of rockburst dynamic disaster. (c) Combined with the energy evolution characteristics of specimen under different loading rates, the initial compression stage elastic strain energy growth rate is greater than the growth rate of dissipation energy before the peak, and the majority of the external energy input is converted into elastic energy. In the postpeak failure stage, the elastic energy is released rapidly, the dissipation energy increases at a higher rate, and all the external energy input is converted into post-peak dissipation energy. This implies that the greater the loading rate, the amount of energy accumulated before the specimen failure is stored in the specimen in the form of elastic energy, the greater amount of energy released after the specimen destruction.

4.3.2. Conversion Rate of Energy Eigenvalues of Specimens with Different Loading Rates. The ratio of total energy increment ΔU, elastic strain energy increment ΔU_e, and dissipative energy increment ΔU_d to the corresponding time increment Δt of specimen between the loading-unloading onset point and the peak stress point is defined as the total energy conversion rate u, the elastic strain energy conversion rate u_e, and the dissipative energy conversion rate u_d [19, 20], respectively. The calculation expression is given as follows:

$$\begin{cases} u = \dfrac{\Delta U}{\Delta t}, \\ u_e = \dfrac{\Delta U_e}{\Delta t}, \\ u_d = \dfrac{\Delta U_d}{\Delta t}. \end{cases} \tag{3}$$

The energy conversion rates of specimen with different loading rates are shown in Figure 9. The mathematical expressions of u and loading rate are shown in Table 5; where, r is the loading rate.

As shown in Figure 9 and Table 5, (a) The correlation coefficient values for each energy eigenvalue conversion rate and loading rate are greater than 0.92, indicating a strong linear correlation between the two. The total energy conversion rate u, the elastic strain energy conversion rate u_e, and the dissipative energy conversion rate u_d are positively correlated with the loading rate. It indicates that as the loading rate increases, more energy is input to the specimen from the outside, the rock mainly undergoes shear failure, and the generation of shear cracks requires a high amount of energy consumption, resulting in a higher percentage of dissipative energy in the rock. (b) As the loading rate increases, the elastic strain energy accumulated inside the specimen increases, and as the external loading continues to grow, the resulting force is dispersed, resulting in a distinct type of energy transformation. This indicates that when the sum of external energy input to the specimen and the elastic strain energy release is greater than the dissipated energy required for rock fragmentation, the excess energy will be released as kinetic energy of fragments, specifically as loosening, spalling, throwing, or ejection of fragments. (c) Translating the loading rate at the test room scale into the working face boring rate during the underground cavity excavation should reduce the concentration of vertical stress in the tunnel surrounding rock mass, improve the bearing capacity of surrounding rock mass, control the deformation of surrounding rock mass, and enhance the stability of surrounding rock mass in order to lessen the seriousness of rockburst.

5. Numerical Simulation Analysis

5.1. Generation of Crystal Scale Fine Model

5.1.1. Geometry Model. Granite is a natural aggregate composed of mineral grains of varying sizes and shapes that have been accumulated by geological processes in

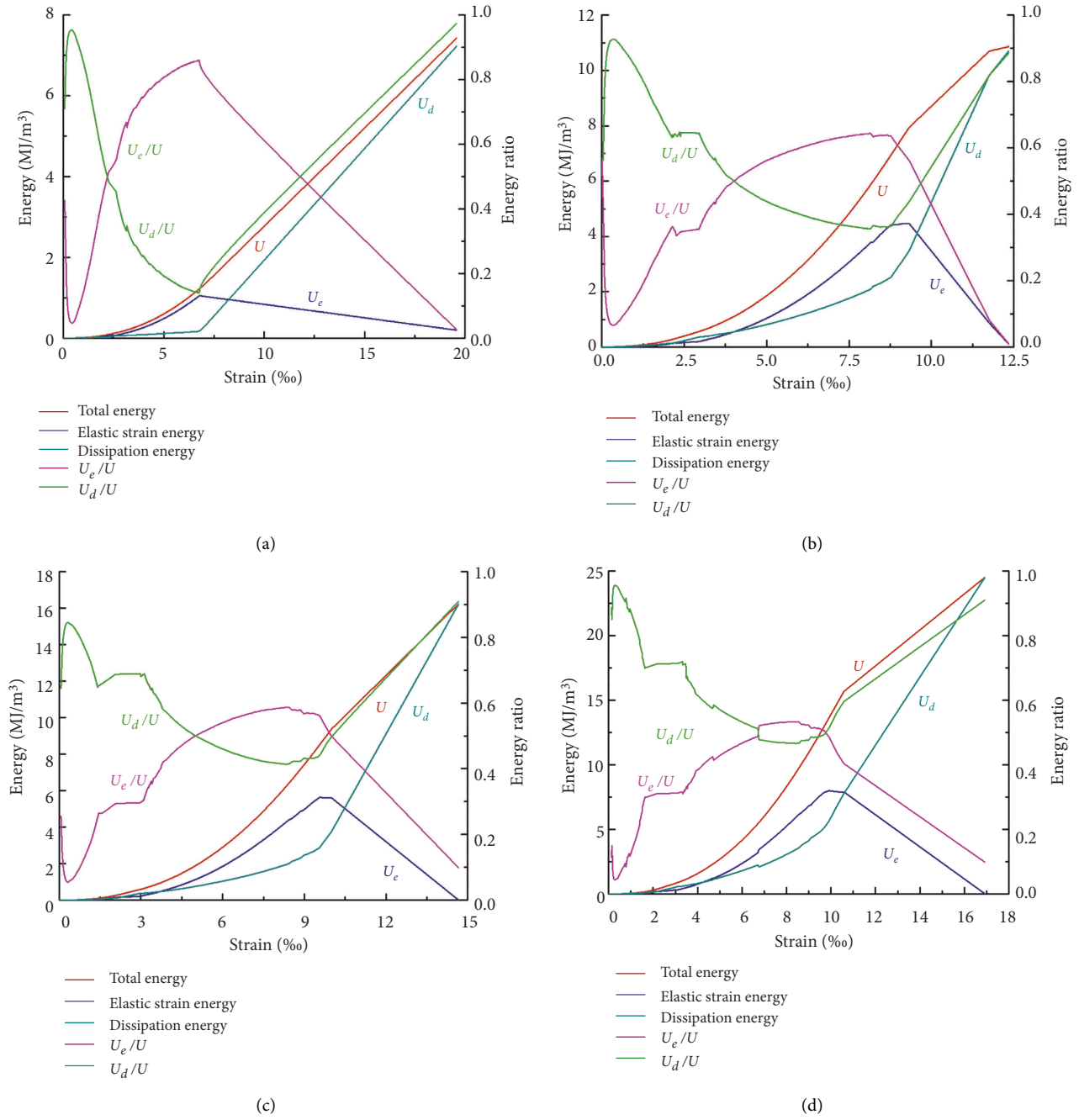

Figure 8: Energy transformation characteristics of specimen with different loading rates during rockburst. (a) 0.05 MPa/s; (b) 1.0 MPa/s; (c) 3.0 MPa/s; and (d) 5.0 MPa/s.

Table 4: Energy values at peak stress with different loading rates.

Loading rate (MPa/s)	U (MJ/m^3)	U_e (MJ/m^3)	U_d (MJ/m^3)	U_e/U	U_d/U
0.05	1.324	1.040	0.284	0.785	0.215
1.0	7.947	4.464	3.483	0.562	0.438
3.0	8.506	4.729	3.777	0.556	0.444
5.0	13.660	7.001	6.659	0.513	0.487

accordance with particular laws. The grains that makeup granite rocks resemble polygons; hence, the polygon mesh is more consistent with the internal fine structure characteristics of the rock. With the help of 3D Voronoi subdivision profile technology and regularization technology, a crystal scale fine model (CSFM) is built that accurately

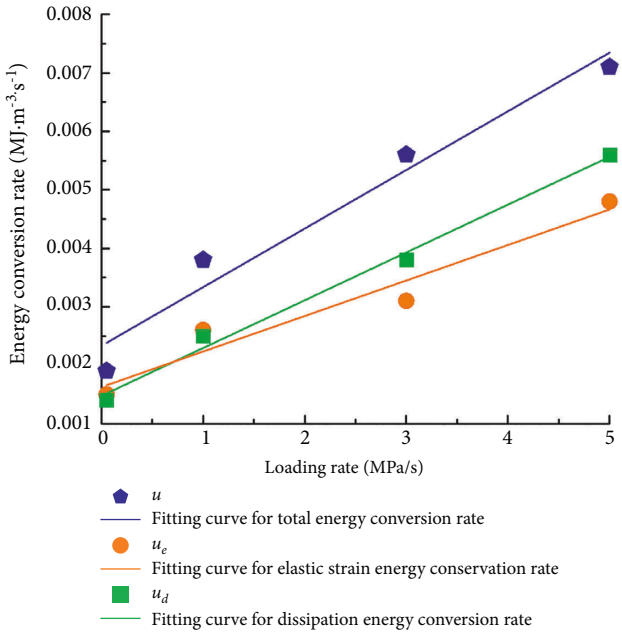

Figure 9: Energy conversion rate of specimen with different loading rates during rockburst.

Table 5: Mathematical expression of u and loading rate.

Energy conversion rate	Fitting curve	Correlation coefficient
u	$u = 0.0010r + 0.0020$	0.9620
u_e	$u_e = 0.0006r + 0.0016$	0.9472
u_d	$u_d = 0.0008r + 0.0015$	0.9924

represents the mineral grain composition. The CSFM is embedded into the secondary development block discrete element software platform by compiling the NEPER-DEM data interface calculation program using the FISH language embedded. The entire process of rockburst inoculation-occurrence-development and the energy evolution characteristics under true triaxial single face unloading conditions were studied. The simulation of interaction between mineral grains and failure process of microfracture eruption, expansion, and penetration will shed additional light on the rockburst formation mechanism.

Using a polarization microscope, the lithology and mineral composition of rock sample sections were determined. The granite specimen used in this study is mostly composed of potassium feldspar (48%), quartz (39%), plagioclase (8%), and black mica (5%). Due to the high content of quartz minerals and the brittle and hard texture, the granite sample has a material basis for brittle failure. The three-dimensional crystal scale fine model is shown in Figure 10.

5.1.2. Failure Criterion and Calibration Micro-Parameters. Crystal-scale cracks emerging from interparticle contact failure of CSFM can be further classified as tensile and shear cracks based on their fracture mechanisms. When the normal tensile stress of particles within a mineral crystal exceeds the tensile strength, tensile failure occurs in interparticle contact and produces intracrystalline tensile cracks. When the tangential shear stress of particles within a mineral crystal exceeds the shear strength, shear failure occurs in interparticle contact and produces intracrystalline shear cracks. This work uses the maximum tensile strain criterion and the SMP criterion to determine the methodologies for determining tensile and shear failure of the contact surface.

In this paper, Weibull distribution functions are introduced to describe the rock and joint mechanical parameters. A data interface program is prepared in FISH language to assign multiple sets of lithological parameters conforming to the Weibull distribution to the model. Firstly, an array of coefficients conforming to the Weibull distribution is generated. Secondly, suitable fine mechanical parameters are obtained by the "iterative test method" [21]. Finally, element k is randomly taken from the coefficient array as the Weibull distribution coefficient, and the coefficient k is multiplied by the average value of each component of the parameter to obtain multiple sets of rock mechanics parameters conforming to the Weibull distribution.

Tables 6 and 7 display the fine mechanical parameters of various mineral grains derived from the calibration results [22]. In Table 7, K_n is the contact normal stiffness, K_s is the contact shear stiffness, J_T is the contact tensile strength, J_C is the contact cohesion, and φ_r is the contact residual friction angle.

5.2. Comparison and Analysis of Stress-Strain Curve and Failure Mode of Rock Sample

5.2.1. Comparison and Analysis of Stress-Strain Curve of Rock Sample. Figure 11 compares the axial stress-strain curves of rock samples derived from physical experiments and numerical simulations.

From Figure 11, it is clear that (1) both the test curve and the simulation curve exhibit four stages: the initial compression stage, the elastic deformation stage, the prepeak unstable fracture stage, and the postpeak failure stage, and that the curve change trend is essentially identical. It demonstrates that the discrepancy between numerical calculation results and experimental results is not obvious and that the two curves are in good agreement. (2) As the loading rate increased, the peak strain and peak stress of rock sample exhibited an upward trend. This implies a positive correlation between the loading rate and the peak strain and peak stress of rock sample. Compared with the static brittle failure rock sample no. Z-1, the typical stress-strain curve of rock samples with ejection failure has an obvious yield platform, and the change is gentle and maintains a relatively stable state. (3) Analysis of the macroscopic failure process of rock sample: under the same stress path, the No. Z-1 granite specimen presents static brittle failure by slabbing, whereas the other granite specimens present dynamic failure by rockburst. On the typical stress-strain curves of granite specimens with different grain sizes, five characteristic points ($A \sim E$) were selected to depict the different stages experienced by rock samples during failure process. This

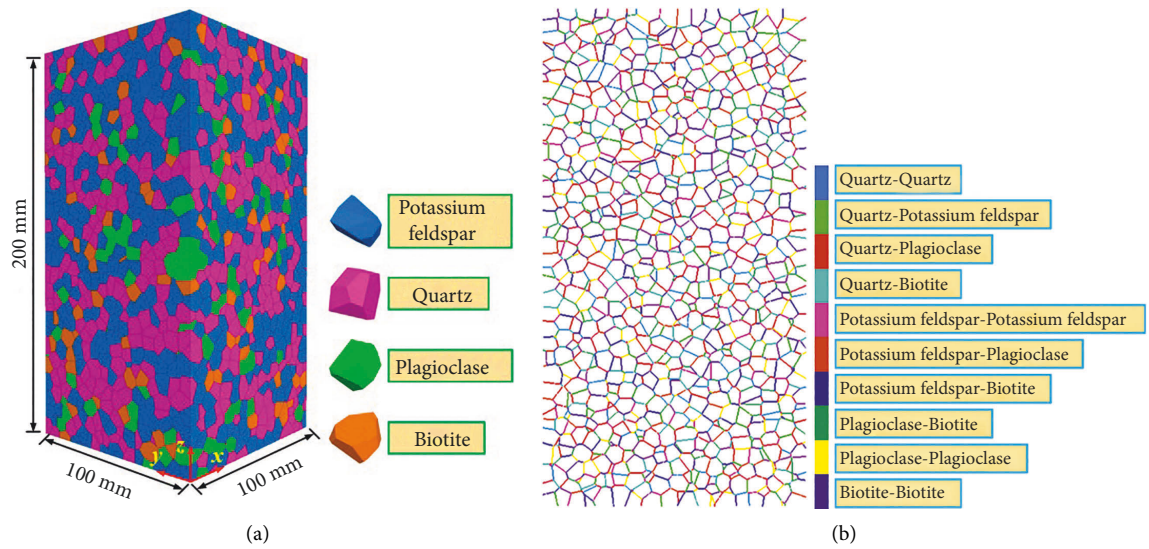

Figure 10: Three-dimensional crystal scale fine model. (a) The 3D numerical rock specimen used with the grains assigned as potassium feldspar (blue), quartz (pink), plagioclase (green), biotite (peach) (as guided by the modal composition of the studied granite, the allocation of minerals is performed in a random manner). The outline of the polyhedral (the grains) can be seen. (b) 2D slice of a cube numerical specimen showing the different grain-to-grain contacts (color figure online).

Table 6: Microscopic parameters of mineral grains.

Mineral composition	Bulk modulus (GPa)	Shear modulus (GPa)	Poisson's ratio
Quartz	38.2	43.3	0.20
Potassium feldspar	55.6	29.5	0.25
Plagioclase	45.6	27.3	0.26
Biotite	59.7	42.3	0.27

Table 7: Microscopic parameters of grain contacts.

Contact	K_n (GPa/mm)	K_s (GPa/mm)	J_T (MPa)	J_C (MPa)	φ_r (°)
Quartz-quartz	836	418	47.69	201	8
Quartz-potassium feldspar	561	281	46.31	198	8
Quartz-plagioclase	502	251	32.59	187	9
Quartz-biotite	452	226	46.36	179	7
Potassium feldspar-potassium feldspar	365	183	52.26	169	8
Potassium feldspar-plagioclase	469	235	45.46	185	9
Potassium feldspar-biotite	359	180	32.15	179	9
Plagioclase-plagioclase	452	225	30.26	194	8
Plagioclase-biotite	587	294	29.68	161	7
Biotite-biotite	550	275	61.57	171	8

further verifies that the numerical simulation is in good agreement with the failure process variation of experimental test.

5.2.2. Comparison and Analysis of Failure Mode of Rock Sample. Figure 12 depicts a comparison between numerical simulation and experimental results for the ultimate failure modes of rock samples.

From Figure 12, it can be seen that (1) The characteristics of rock sample failure mode obtained from the numerical simulation under different loading rates are essentially the same as the results of experimental test. It indicates that the crystal scale fine model can better simulate the main macroscopic cracks that lead to the final failure of rock sample, particularly in the final failure mode of specimen, which demonstrates a high degree of agreement with the experimental test. (2) The numerical simulation reveals that the failure modes of rock samples primarily consist of tensile, shear, and tensile-shear composite failure. As the loading rate increases, the depth, and volume of rockburst pits increase, the splitting fractures become more fully developed, the penetration of shear diagonal fractures increases, and the shear failure activity within the seam intensifies, which is consistent with the results of experimental tests. (3) In addition, the failure modes of rock samples produced from numerical simulations are comparable to those of experimental tests, which further verifies the

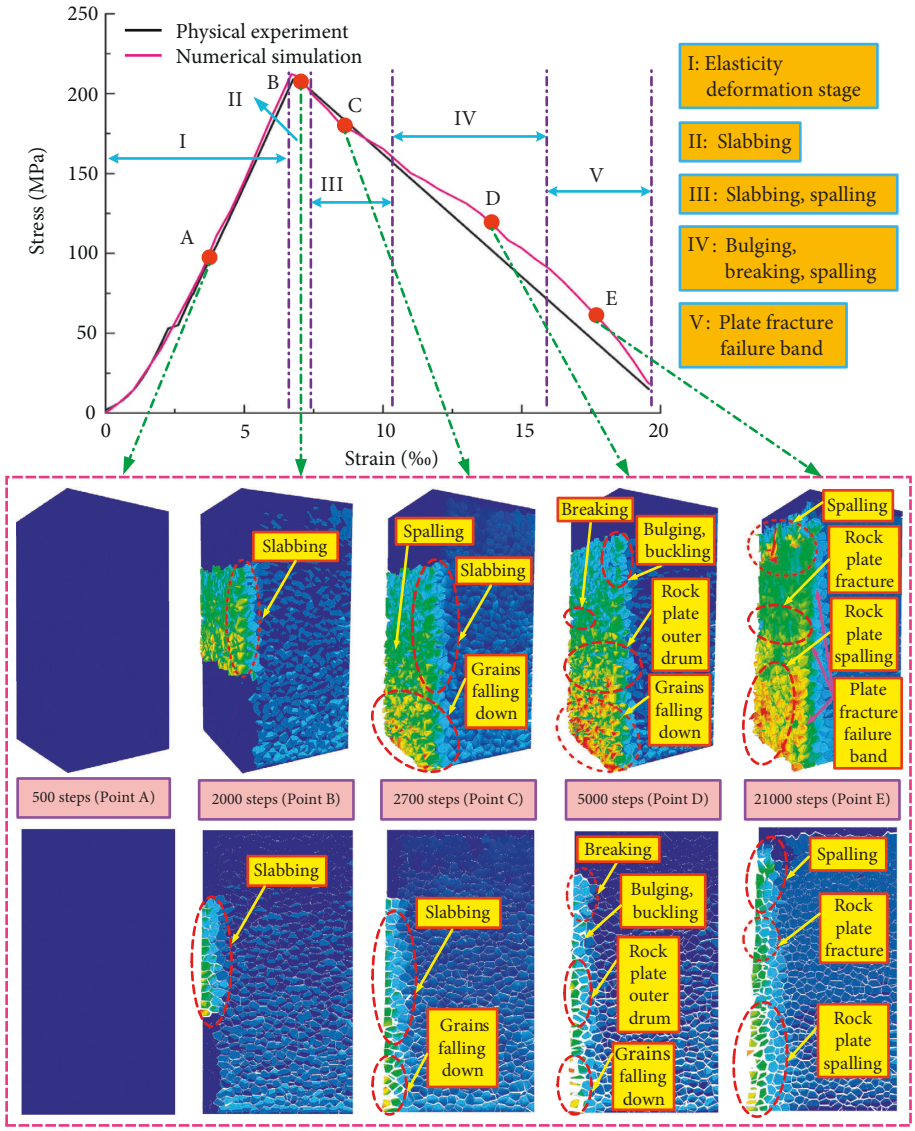

(a)

Figure 11: Continued.

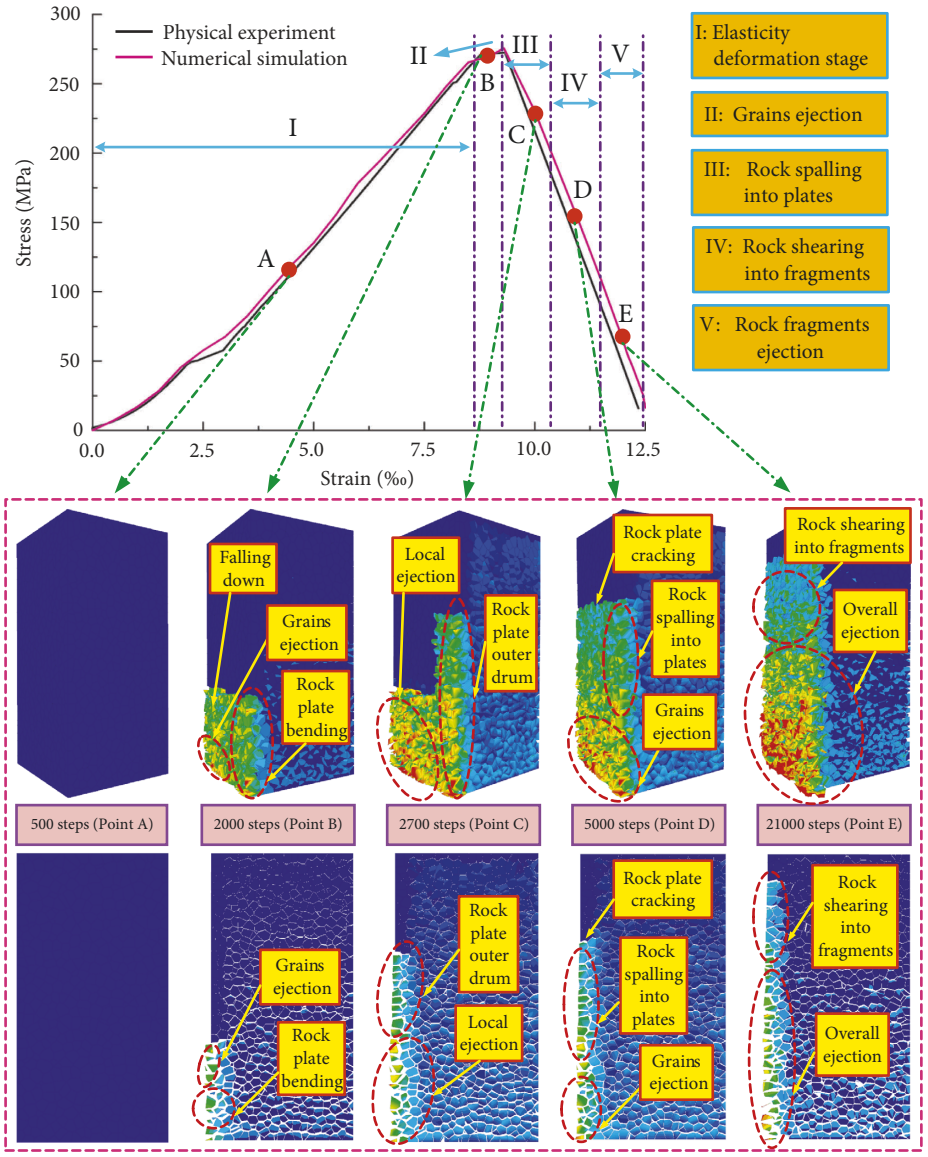

(b)

Figure 11: Continued.

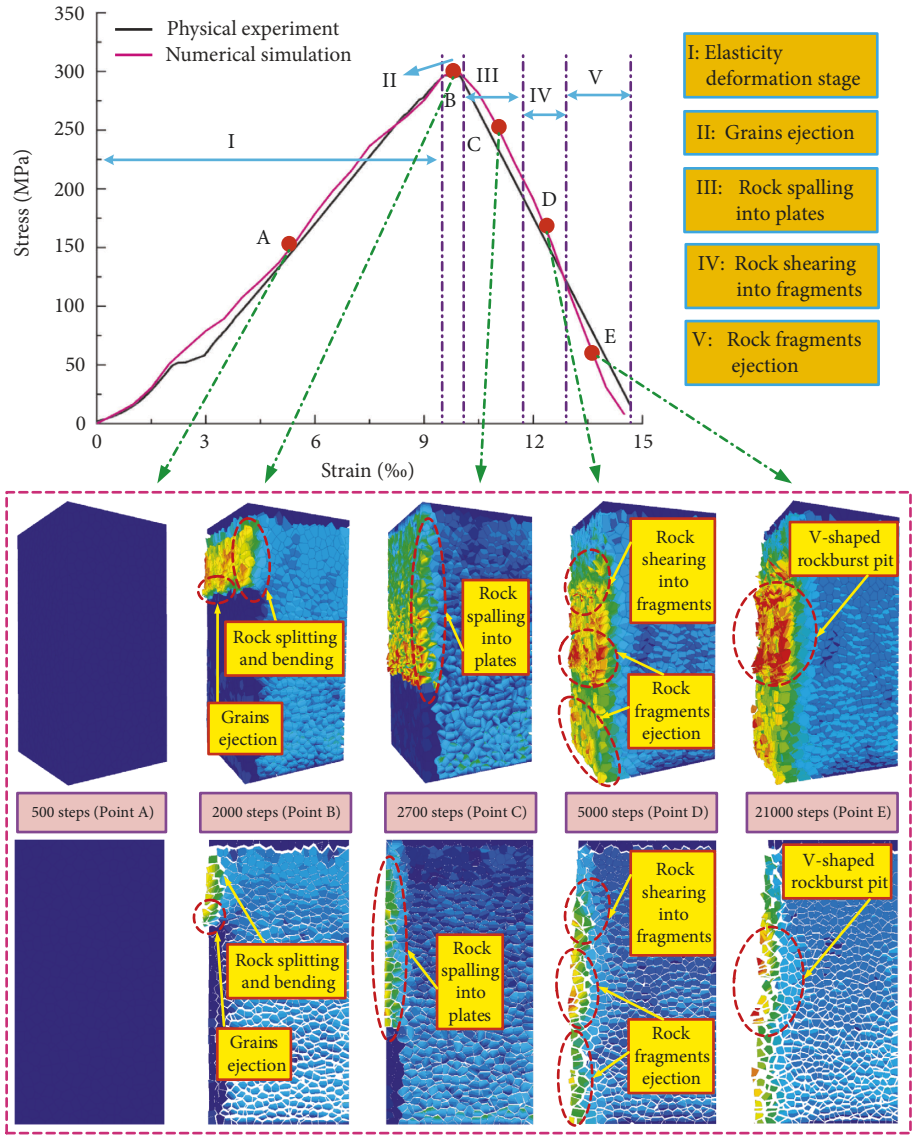

(c)

Figure 11: Continued.

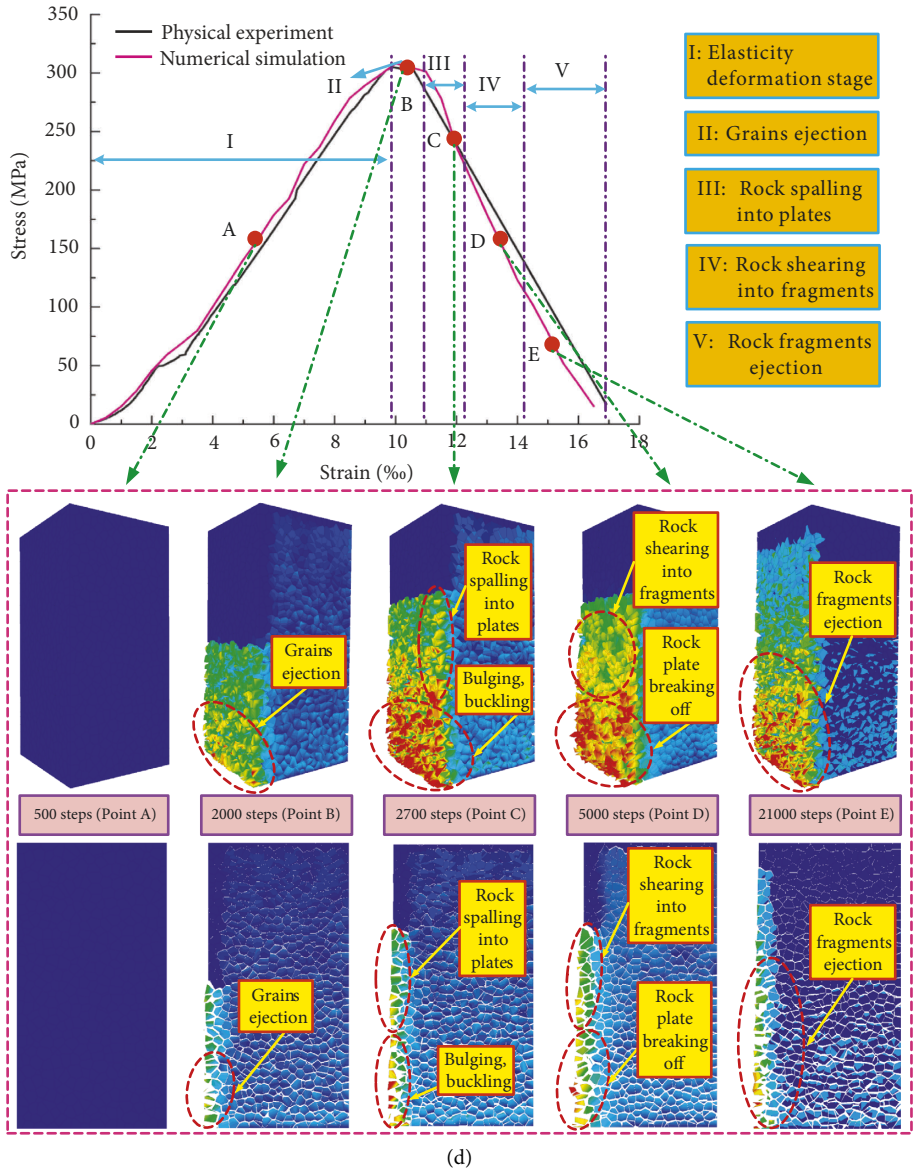

Figure 11: Numerical simulation and physical experiment stress-strain curve comparison and three-dimensional ejection photographs and corresponding central section of typical points (A–D). (a) 0.05 MPa/s; (b) 1.0 MPa/s; (c) 3.0 MPa/s; and (d) 5.0 MPa/s.

rationality of introduction of Weibull distribution function to describe the mechanical parameters of rock blocks and joints in this paper. The abovementioned also shows great agreement with the experimental results.

5.3. Loading Rate Effect on Evolution Process of Energy. The numerical calculation program is compiled by the FISH language embedded in the 3D discrete element software in order to monitor the elastic strain energy of each unit and the ejection kinetic energy of each block in real-time. Figure 13 shows the evolution process of the stored elastic strain energy and released kinetic energy of specimen with different loading rates.

According to Figure 13 and related data, we can find that: (1) the trends of elastic strain energy curves derived from experimental tests (Figure 6) and numerical simulations are essentially identical. The higher the loading rate, the more elastic strain energy is stored, and the limit of energy storage for specimens with loading rates of 1.0/3.0/5.0 MPa/s is 3.63 times, 4.59 times, and 5.56 times that for specimens with loading rates of 0.05 MPa/s, respectively. On the other hand, the growth rate of elastic energy of granite specimens in each group differs greatly, and the higher the loading rate, the faster the growth rate of elastic energy. (2) The ejection kinetic energy of specimens with different loading rates varied greatly. The ejection kinetic energy of specimens with loading rate of 5 MPa/s was significantly greater than that of other specimens. The final ejection kinetic energy of specimens with loading rate of 0.05/1.0/3.0 MPa/s decreased by 76.55%, 33.78%, and 6.76%, respectively, when compared to that of the specimens with loading rate of 5 MPa/s. This is

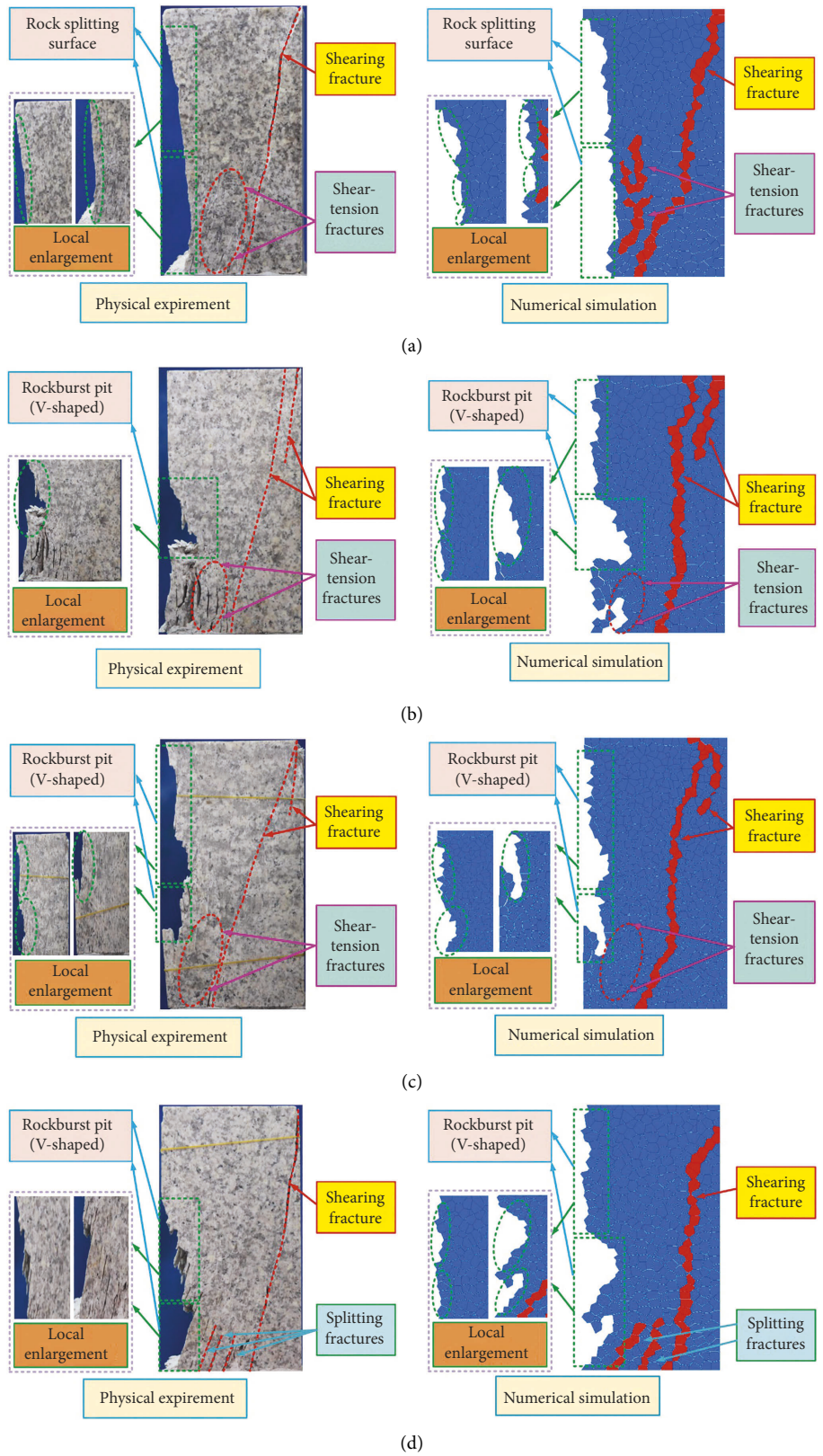

Figure 12: Comparison of rock specimen ultimate failure modes between experiment and simulation. (a) 0.05 MPa/s; (b) 1.0 MPa/s; (c) 3.0 MPa/s; and (d) 5.0 MPa/s.

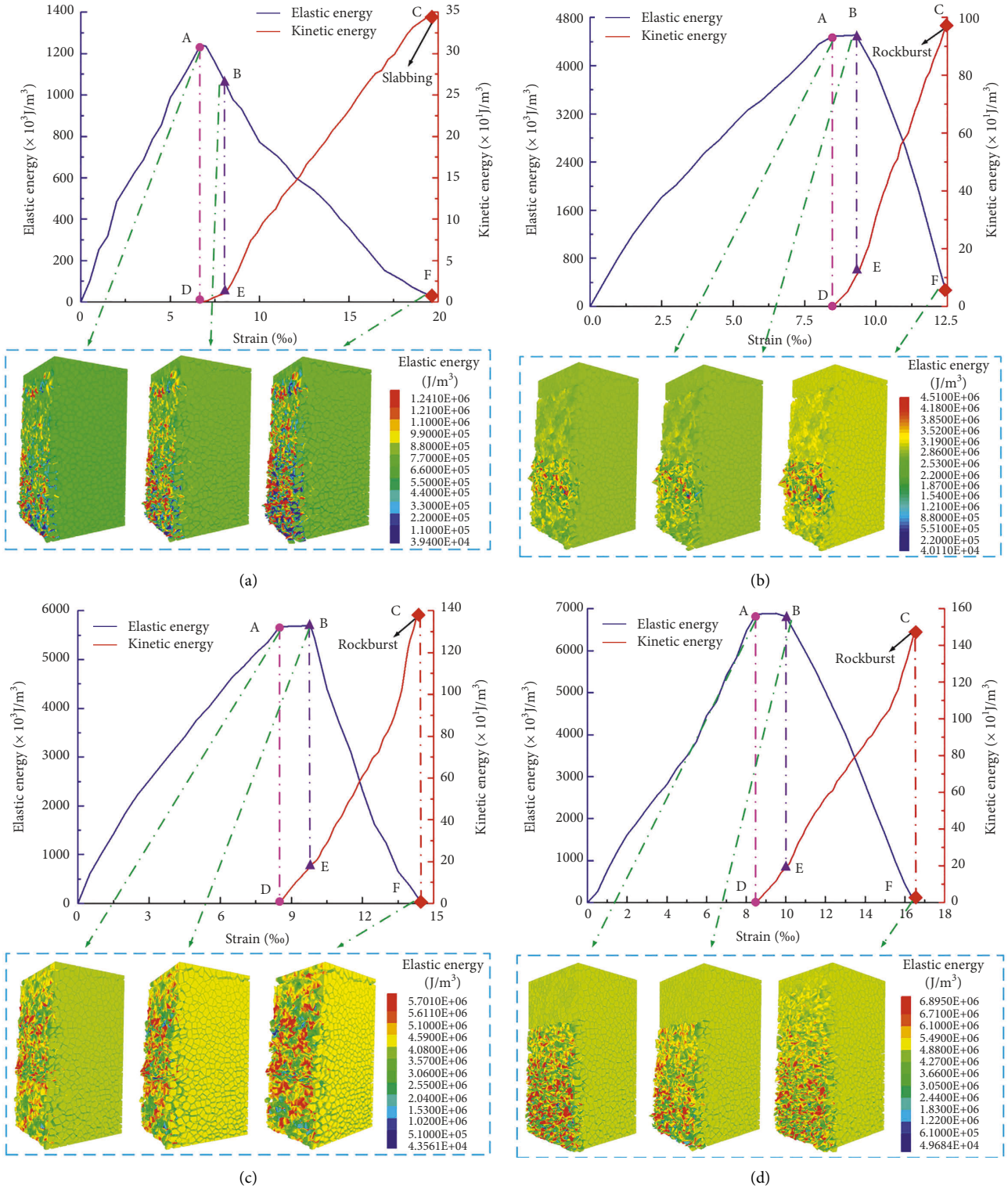

FIGURE 13: Evolution process of the stored elastic energy and released kinetic energy of specimen with different loading rates. (a) 0.05 Mpa/s; (b) 1.0 Mpa/s; (c) 3.0 Mpa/s; and (d) 5.0 MPa/s.

also the reason why 5 MPa/s loading rate specimens failure modes appeared relatively more ejected fragments of energy. (3) The elastic energy change curves of specimens subjected to loading rates of 1.0/3.0/5.0 MPa/s all contain two inflection points. These two inflection points correspond to the starting and ending points (points *A* and *B*) of the yield platform, respectively. The evolution of elastic energy grows approximately linearly at a low rate between the two inflection points (points *A* and *B*), while the evolution of kinetic energy grows approximately linearly at a high rate

between the D point and E point. The characteristics of the existing two inflection points and the high rate linear growth of kinetic energy evolution between point D and point E can provide precursor information for rockburst prediction. The kinetic energy is released abruptly in the postpeak stage, and at the moment of the elastic energy drops sharply, the kinetic energy suddenly increases from zero to a high value (points C and F). (4) The overall trends of elastic energy curves for specimens loaded at 1.0/3.0/5.0 MPa/s are similar, and the elastic energy decreases sharply after reaching its peak. The elastic energy curve of specimens loaded at 0.05 Mpa/s exhibited a sharp increase followed by a gradual drop.

6. Conclusions

(1) The energy evolution process of specimens under different loading rates can be summed up in four stages: the initial compression stage, the elastic deformation stage, the prepeak unstable fracture stage, and the postpeak failure stage. Among them, energy accumulation mainly occurs in the initial compression stage and elastic deformation stage, energy dissipation mainly occurs in the prepeak unstable fracture stage, and energy release mainly occurs in the postpeak failure stage. With the increase in loading rate, the specimen is in the process of energy accumulation accompanied by energy dissipation, more external input energy, and elastic strain energy released into the kinetic energy of breaking rock block, resulting in rockburst phenomenon.

(2) As loading rate increases, the elastic strain energy conversion rate (U_e/U) drops, whereas the dissipative energy conversion rate (U_d/U) increases. The higher the elastic strain energy conversion rate and the lower the dissipative energy conversion rate, resulting in a more powerful rockburst. The loading rate at the laboratory scale into the underground cavity excavation process of working face driving rate. It should reduce the excavation cycle footage, improve the bearing capacity of surrounding rock mass, control the deformation of surrounding rock mass, and increase the stability of surrounding rock mass in order to reduce the intensity of rockburst and delay its occurrence of rockburst.

(3) Using a three-dimensional discrete element numerical simulation platform, the entire process of inoculation-occurrence-development of rockburst was successfully simulated, supporting the conclusions of experimental physical testing. At a loading rate of 0.05 MPa/s, rock samples had static brittle failure by slabbing, at loading rates of 1.0/3.0/5.0 MPa/s, rock samples experienced varying degrees of rockburst failure. The rockburst ejection failure process can be summarized as four stages: grains ejection, rock spalling into plates, rock shearing into fragments, and rock fragments ejection. The failure mode of rockburst demonstrates multiplicity, that is, the unloading face appears as a rockburst pit due to tensile-shear failure, and splitting fractures due to tension, while the inside of the rock body appears as a penetrating shear fracture due to shear failure.

(4) The overall trend of elastic energy curves of specimens with loading rates of 1.0/3.0/5.0 MPa/s is relatively similar, with the elastic energy showing a sharp decrease after reaching the peak. The elastic energy curve of specimens with a loading rate of 0.05 MPa/s showed a sharp increase and then a slow decrease. The kinetic energy is released abruptly in the postpeak stage, and at the moment of the elastic energy drops sharply, the kinetic energy suddenly increases from zero to a high value. The high rate linear growth of kinetic energy evolution between the two inflection points can provide precursor information for rockburst prediction.

Data Availability

The data presented in this study are available on request from the corresponding author.

Conflicts of Interest

The authors declare that the research was conducted in the absence of any commercial or financial relationships that could be construed as potential conflicts of interest.

Acknowledgments

This research was funded by the National Natural Science Foundation of China (Grant nos. 52178388 and U1810203) and Natural Science Foundation of Henan Province (Grant no. 212300410146).

References

[1] M. Q. You and A. Z. Hua, "Energy analysis on failure process of rock specimens," *Chinese Journal of Rock Mechanics and Engineering*, vol. 21, no. 6, pp. 778–781, 2002.

[2] H. P. Xie, R. D. Peng, and Y. Ju, "Energy dissipation of rock deformation and fracture," *Chinese Journal of Rock Mechanics and Engineering*, vol. 23, no. 21, pp. 3565–3570, 2004.

[3] R. Yang, L. Jiakun, B. Zhou, and D. P. Ma, "Rock unloading failure precursor based on acoustic emission parametric fractal characteristics," *Lithosphere*, no. 11, Article ID 8221614, 2022.

[4] Z. Y. Chen, G. S. Su, J. W. Ju, and J. Q. Jiang, "Experimental study on energy dissipation of fragments during rockburst," *Bulletin of Engineering Geology and the Environment*, vol. 78, no. 7, pp. 5369–5386, 2019.

[5] C. P. Polito and H. H. M. Moldenhauer, "Energy dissipation and pore pressure generation in stress-and strain-controlled cyclic triaxial tests," *Geotechnical Testing Journal*, vol. 42, no. 4, pp. 20170437–20171089, 2019.

[6] R. D. Weyher, M. K. McCarter, and J. M. Wempen, "Energy partitioning following tensile failure in three-point loading tests of nugget sandstone specimens," *Mining, Metallurgy & Exploration*, vol. 37, no. 5, pp. 1499–1515, 2020.

[7] J. Lu, D. M. Zhang, G. Huang, X. Li, H. Gao, and G. Z. Yin, "Effects of loading rate on the compound dynamic disaster in

deep underground coal mine under true triaxial stress," *International Journal of Rock Mechanics and Mining Sciences*, vol. 134, Article ID 104453, 2020.

[8] X. F. Si, L. Q. Huang, F. Q. Gong, X. L. Liu, and X. B. Li, "Experimental investigation on influence of loading rate on rockburst in deep circular tunnel under true-triaxial stress condition," *Journal of Central South University*, vol. 27, no. 10, pp. 2914–2929, 2020.

[9] X. P. Zhang, Y. J. Jiang, G. Wang, J. C. Wang, X. Z. Wu, and Y. Z. Zhang, "Numerical experiments on rate-dependent behaviors of granite based on particle discrete element model," *Rock and Soil Mechanics*, vol. 37, no. 9, pp. 2679–3686, 2016.

[10] S. Lee, K. Ramos, and K. Matous, "Numerical study of damage in particulate composites during high-strain rate loading using novel damage model," *Mechanics of Materials*, vol. 160, Article ID 103944, 2021.

[11] Q. Ma, Y. L. Tan, X. S. Liu, Z. H. Zhao, D. Y. Fan, and L. Purev, "Experimental and numerical simulation of loading rate effects on failure and strain energy characteristics of coal-rock composite samples," *Journal of Central South University*, vol. 28, no. 10, pp. 3207–3222, 2021.

[12] L. Q. ., . Yu, Q. L. Yao, Q. Xu, W. N. Wang, Z. J. Niu, and W. D. Liu, "Experimental and numerical simulation study on crack propagation of fractured fine sandstone under the influence of loading rate," *Journal of China Coal Society*, vol. 46, no. 11, pp. 3488–3501, 2021.

[13] C. E. Fairhurst and J. A. Hudson, "Draft ISRM suggested method for the complete stress-strain curve for intact rock in uniaxial compression," *International Journal of Rock Mechanics and Mining Sciences*, vol. 36, no. 3, pp. 279–289, 1999.

[14] B. R. Chen, X. T. Feng, H. J. Ming et al., "Evolution law and mechanism of rockburtst in deep tunnel: time delayed rockburst," *Chinese Journal of Rock Mechanics and Engineering*, vol. 31, no. 3, pp. 561–569, 2012.

[15] X. C. Hu, G. S. Su, G. Y. Chen et al., "Experiment on rockburst process of borehole and its acoustic emission characteristics," *Rock Mechanics and Rock Engineering*, vol. 52, no. 3, pp. 783–802, 2019.

[16] G. S. Su, J. Q. Jiang, S. B. Zhai, and G. L. Zhang, "Influence of tunnel axis stress on strainburst: an experimental study," *Rock Mechanics and Rock Engineering*, vol. 50, no. 6, pp. 1551–1567, 2017.

[17] X. R. Ge and M. X. Hou, "A new 3D in-situ rock stresses measuring method: borehole wall stress relief method (BWSRM) and development of geostress measuring instrument based on BWSRM and its primary applications to engineering," *Chinese Journal of Rock Mechanics and Engineering*, vol. 30, no. 11, pp. 2161–2180, 2011.

[18] H. P. Xie, Y. Ju, and L. Y. Li, "Criteria for strength and structural failure of rocks baded on energy dissipation release principles," *Chinese Journal of Rock Mechanics and Engineering*, vol. 24, no. 17, pp. 3003–3010, 2005.

[19] D. Huang and Y. R. Li, "Conversion of strain energy in triaxial unloadingtests on marble," *International Journal of Rock Mechanics and Mining Sciences*, vol. 66, no. 1, pp. 160–168, 2014.

[20] G. Z. Yin, B. Ma, C. Liu, M. H. Li, J. Lu, and S. Y. Yin, "Effect of loading and unloading rates on mechanical properties and energy characteristics of sandstone under true triaxial stress," *Journal of China Coal Society*, vol. 44, no. 2, pp. 454–462, 2019.

[21] X. F. Li, H. B. Li, and J. Zhao, "3D polycrystalline discrete element method (3PDEM) for simulation of crack initiation and propa-gation in granular rock," *Computers and Geotechnics*, vol. 90, pp. 96–112, 2017.

[22] T. Xu, T. F. Fu, M. J. Heap, P. G. Meredith, T. M. Mitchell, and P. Baud, "Mesoscopic damage and fracturing of heterogeneous brittle rocks based on three-dimensional polycrystalline discrete element method," *Rock Mechanics and Rock Engineering*, vol. 53, no. 12, pp. 5389–5409, 2020.